Available online at www.sciencedirect.com

ScienceDirect

Journal of Terramechanics 59 (2015) 59–70

Journal of Terramechanics

www.elsevier.com/locate/jterra

A hybrid force model to estimate the dynamics of curved legs in granular material

Lichao Xu, Shiwu Zhang *, Nan Jiang, Ronald Xu

Dept. of Precision Machinery and Precision Instrumentation, University of Science and Technology of China, Hefei, Anhui 230026, China

Received 25 August 2014; received in revised form 24 March 2015; accepted 26 March 2015
Available 11 April 2015

Abstract

Robot locomotion on rigid terrain or in fluids has been studied to a large extent. The locomotion dynamics on or within soft substrates such as granular material (GM) has not been fully investigated. This paper proposes a hybrid force model to simulate and evaluate the locomotion performance of a legged terrestrial robot in GM. The model incorporates an improved Resistive Force Theory (RFT) model and a failure-based model. The improved RFT model integrates the force components of individual leg elements over the curved leg portion submerged in GM at any moment during a full period of leg rotation. The failure-based model is applied in a bar drag model to yield the normal and the lateral forces of the individual RFT elements as functions of the locomotion depth and speed. The hybrid model is verified by the coincidence between the theoretical predictions and the experimental results. The hybrid model is used to analyze the effects of angular velocity and leg shape with high precision and can guide the design of the legs with any profiles. Our study reveals that the interactions between locomotor and substrate are determined by the locomotor structural characteristics, the nature of the substrate, and the control strategy.

Keywords: Terrestrial robots; Locomotion; Hybrid force model; Dynamics; Granular material

1. Introduction

Developing robots able to overcome complex environments has aroused more and more interests. A number of research groups have done excellent work on exploring robot locomotion in solid, liquid, and the transitional environments (Saranli et al., 2001; Raibert et al., 2008; Crespi et al., 2013; Boxerbaum et al., 2005; Dudek et al., 2007). Understanding dynamics of locomotors in soft substrates is significant to improve the locomotory performance of the robots in terrains such as desert and beach. Generally, there are two methods to explore the interaction between robots and terrains. One is through semiempirical equations based on well-known pressure-sinkage model (Bekker, 1969) and shearing stress-displacement model (Janosi and Hanamoto, 1961), which has been widely used in design of locomotors and soil mechanics prediction (Asnani et al., 2009; Ding et al., 2013; Iagnemma et al., 2004; Ding et al., 2013; Patel et al., 2004). The other method is mainly through FEM or DEM simulation based on different contact models (Xia, 2011; Fervers, 2004; Smith and Peng, 2013), these works also promoted the in-depth understanding of material properties and their interaction with robots. However, the limitation of the existing models generally cannot be applied when the locomotors semi-submerge in loose terrain (Terzaghi, 1943), and the parameters in simulation model have to be carefully adjusted to reflect the practical situation. Considering this, robot locomotion in granular materials (GMs) is still in need of extensively study. Compared with solid and liquid materials, GMs show elastic deformation

* Corresponding author.
E-mail address: swzhang@ustc.edu.cn (S. Zhang).

http://dx.doi.org/10.1016/j.jterra.2015.03.005
0022-4898/

Nomenclature

σ	normal stress (Pa)
τ	tangential stress (Pa)
F_f	forward advancing force (N)
F_s	supportive force (N)
T	torque (N m)
γ	density of GM (g/cm^3)
h	height of the fixed motor axle (cm)
h_1	depth of bar (cm)
h_0	width of bar (cm)
L_s	subsurface part length of curved leg (cm)
β	angle of direction of $F_\perp$(°)
F_z	lift force on the bar (N)
ξ	angular position of element (rad)
d	submerging depth of element (cm)
ω	angular velocity of the leg (rad/s)
v	speed vector of element/bar (rad/s)
$F_\perp$	normal force component (N)
$F_\parallel$	tangential force component (N)
$C_\perp$	maximum $F_\perp$ (N)
$C_\parallel$	maximum $F_\parallel$ (N)
W_1, W_2	weight of GM in active/passive failure state (N)
a, b	axis of elliptical legs
ϕ, ϕ_w	friction angle within sand/between sand and bar (rad)
r	distance from element to rotating axle (mm)
M_x, M_y	torque caused by dF_f and dF_s (N m)
α_1, α_2	angle between active/passive failure plane and x -axis negative direction (rad)
X_1, X_2	forces among sands in various states (N)
P, P_w	force between bar and sands in passive failure region/force on sands in active failure region (N)
k, λ	coefficient for variation of GM bulk density (-)
ψ	angle from v to tangential direction of element (°)

below the yield limit and different rheological properties when destructed (Terzaghi, 1943; Kadanoff, 1999).

Some researchers have revealed GMs failure characteristics as well as the dynamics of intruders of regular shape moving in GMs. For example, Nedderman described the statics and the kinematics of GMs in a container (Nedderman, 2005); Albert et al. studied the forces applied to a cylinder as it was dragged in a GM at a low speed (Albert et al., 1999); Camorra et al. analyzed the projectile impact for improved calibration in particle dynamics simulation (Ciamarra et al., 2004). Recently, Maladen et al. proposed the "Resistive Force Theory" (RFT) to model the undulatory swimming of a sandfish lizard (Goldman et al., 2009). Despite these efforts, it is still difficult to estimate the interaction forces between the locomotion mechanisms and the substrate, which is crucial for the locomotion performance of desert robots, amphibious robots or planetary robots in GM environments (Goldman et al., 2009; Liang et al., 2012; Knuth et al., 2012; Zhang et al., 2013; Gao et al., 2012). One obstacle is that the locomotion of the robot legs with complex shapes in GM involves varying intruding depths and directions that can hardly calculated through a limited number of experiments.

In this paper, a hybrid force model that incorporates an improved RFT model and a failure-based model is proposed to explore the leg–GM interaction with a relatively high precision. The failure-based model calculates the forces on a dragged bar within GM at a low speed. With minor modifications, it can also be applied to move within GM at a high speed. By combining the failure-based model with an improved RFT model, one can conveniently estimate the forces applied to the locomotors as they penetrate in GM. The proposed hybrid model needs only a limited number of parameters that are readily measurable, as evidenced by our experiments. It is also observed that the angular velocity contributes negligibly to the leg–GM interaction within a certain working range. With such simplification, the forces and torques applied to different types of semi-elliptical legs are calculated in order to reveal the performance dependence of robot locomotion and guide the leg shape design. A major advantage of the proposed model is that it considers the macroscopic effect of force chains in the GM environment without the need to include the complicated microscopic parameters, such as the origination and the transmission of the forces among granular particles. In summary, this study forms the basis for leg–GM interaction analysis and may further guide the design of the robot legs for optimal locomotion performance in a GM environment.

2. Materials and methods

The locomotion performance of a terrestrial robot is determined by the propulsion modes associated with the structure of the locomotors. Two common types of locomotion structures are wheels and legs. As a popular man-made locomotion mechanism, the wheel is designed to accomplish many daily tasks on even terrain, and the wheel–soil interaction has been extensively studied (Asnani et al., 2009; Ding et al., 2013; Iagnemma et al., 2004; Senatore et al., 2013). Legged robots or human beings are able to adapt to rough terrain, and the leg-terrain dynamics is usually analyzed with an inverted pendulum model. Furthermore, the dynamics between straight legs and GMs are also explored with various experiments and simulations (Ding et al., 2013; Liu and Kushwaha, 2010; Yeomans et al., 2013; Scott and Saaj, 2012). As presented by the previous study, both of these two locomotion structures suffer the performance lost in GMs (Lejeune et al., 1998).

2.1. Locomotion mechanisms in GM

The locomotion performance of a wheel in a granular substrate environment differs significantly from that on even ground. In wheeled locomotion, the normal stress σ acting on the edge of the wheel contributes to the most of the supportive force, while the tangential stress τ contributes to the most of the forward advancing force, as sketched in Fig. 1a. In GM cases, this results in the lack of propulsion. In comparison, a human being or a humanoid robot can easily obtain sufficient forward advancing force F_f but thwarted by the subsidence of the leg owing to a small supportive force F_s. Therefore, the locomotion performance of these legs is also unsatisfactory in a GM environment (Fig. 1b). A thorny wheel keeps an appropriate balance between the supportive and the propulsive forces that may eventually enhance the locomotion performance. However, the practical use of a thorny wheel is limited by its complicated structure that may be easily weakened or even invalidated owing to the attachment of the substrate (Bekker, 1956). After considering the advantages and the limitations of a thorny wheel, we believe a curved leg (as sketched in Fig. 1c) should be a better design adopting the advantages and avoiding the disadvantages, by intelligently applying solidification of GM through a simple profile.

The C-shaped (i.e., semicircle) leg is a common curved leg that has been adopted in RHex series robots, such as SandBot for effective locomotion in a GM environment (Goldman et al., 2009). The locomotion velocity of the SandBot robot as functions of the sand packing fraction, the angular velocity and the gait control parameters has been studied in detail. Both experimental observations and numerical simulations have demonstrated the advantages of this leg type (Li et al., 2009; Li et al., 2010). However, its force and torque dynamics have not been fully studied despite their important roles in leg-terrain dynamics. To overcome this limitation, we propose a hybrid model that is able to estimate the force and torque profiles, and further to evaluate the locomotion performance of legs of any shape in GMs (Liang et al., 2012; Xu et al., 2013). This model utilizes an improved RFT model originated from the motion study on a horizontal plane (Maladen et al., 2011) and a failure-based model inspired by experimental observations and Coulomb's failure theory (Nedderman, 2005).

2.2. Improved RFT model

Fig. 2 sketches a curved leg with a fixed motor axle at height h. h is assumed constant because of the following considerations: (1) in the case when the substrate is loosely packed, the robot can be supported with its body resting on the substrate surface, h is constant; (2) in the case when the substrate is closely packed, h will fluctuate during leg penetrating, however, the forces of legs at each moment could also be obtained with a certain h at that moment. Without losing the generality, the leg is represented by an elliptic equation. Similar to an RFT model (Gray and Hancock, 1955), the curved leg is partitioned into infinitesimal elements with the tangential and the normal force components $F_\perp$ and $F_\parallel$ applied by GM (Fig. 2). These force components contribute to the overall forward advancing force F_f, the overall supportive force F_s and the overall torque T exerted by GM. In this model, we neglect the internal forces between infinitesimal elements and the variations of GM packing fraction at different leg locations. With this approximation, F_f, F_s and T can be obtained by integrating force components of individual elements over the part of the leg submerged in GM at any moment during a full period of leg rotation, as shown below:

$$\begin{aligned} F_f(\theta,h) &= \int_{L_s} \left(F_\perp \quad \cos\beta + F_\parallel \sin\beta\right) \mathrm{d}l \\ F_s(\theta,h) &= \int_{L_s} \left(F_\perp \sin\beta - F_\parallel \cos\beta\right) \mathrm{d}l \\ T(\theta,h) &= \int_{L_s} \left(M_x + M_y\right) \mathrm{d}l \end{aligned} \tag{1}$$

with

$$M_x = dF_f(d+h)$$
$$M_y = dF_s(\xi + \theta - \pi/2)$$

where L_s represents the subsurface part of the curved leg, M_x and M_y are the torque caused by F_x and F_y, respectively.

Eq. (1) is able to provide the quasi-static solution for the leg–GM interaction. However, it is difficult to obtain $F_\perp$ and $F_\parallel$ values for each element since they are determined

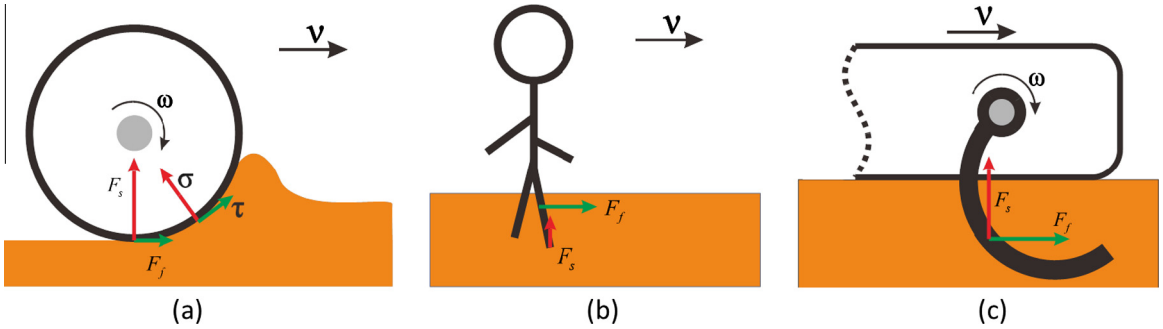

Fig. 1. Illustration of several locomotion modes in a GM environment: (a): wheel, (b): human being, (c): curved leg.

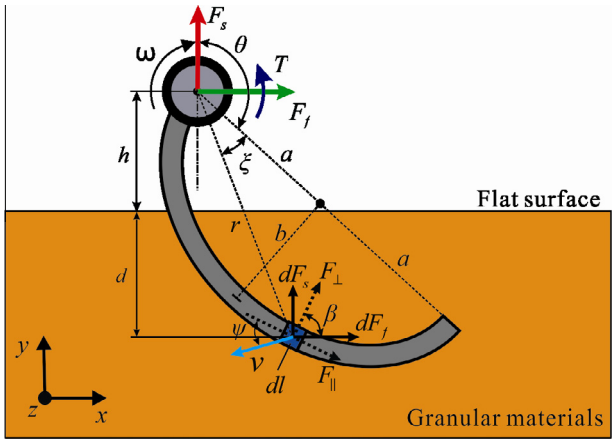

Fig. 2. Schematic of RFT analysis for a semi-elliptical leg penetrating GM at a certain depth. h is the height of the rotation axle above the surface of GM. d is the depth of the element, dl, from GM surface, ξ denotes the angular position of the element. a and b are the long axial radius and the short axis radius of the elliptical leg, respectively. θ denotes the position of the curved leg, which is defined as the angle from the long axle of the elliptical leg to the positive direction along y-axis. $F_\perp$ and $F_\parallel$ are the forces in the tangential direction of the elliptic at the element and the corresponding normal direction, respectively. dF_f and dF_s represent the forces resolved into x-axis direction and y-axis direction respectively. ω represents the angular velocity of the leg. v denotes the speed vector of the element, while ψ denotes the angle between v and the tangential direction of the element. β denotes the angle between $F_\perp$ and dF_f, r denotes the distance from the element to the rotating axle.

by many coupled parameters such as the GM characteristics, the submerging depth of the element, the velocity of the element, and the tangential direction of the elliptical curve at the designated position. Previous studies have examined the drag force applied on a submerged rod that moves horizontally (Kadanoff, 1999; Albert et al., 2000), the forces applied on an inclined plow or a lug during movement in GMs (Yang et al., 2014; Percier et al., 2011), as well as the effect of the locomotor geometry on the resultant forces (Ding et al., 2011). However, no general theory has been established to explain the complicated locomotion dynamics that involves variable penetration depths and directions of the moving elements. We propose an improved RFT model to simulate locomotion dynamics of a curved leg in GM. It is assumed that the forces applied on each element are only relevant to its projected area on the plane perpendicular to its instantaneous velocity direction, velocity magnitude, and depth d. This assumption is based on the analogy between GMs and a low Re fluid in the force origin (Gray and Hancock, 1955; Metcalfe et al., 2002; Lighthill, 1969). With the assumption, the forces $F_\perp$ and $F_\parallel$ can be expressed as following:

$$F_\perp = f_1(\psi, v, d) = f_1(\theta, \xi, \omega)$$
$$F_\parallel = f_2(\psi, v, d) = f_2(\theta, \xi, \omega) \quad (2)$$

Noted that the forces applied to each element are integrated only when $\psi > 0$, as it represents the situation where the moving element is in contact with GM. When $\psi < 0$, the element moves toward the space where the GM has been pushed away by the curved leg in the previous position. To obtain F_f, F_s, and T, a trapezoidal-cross-section bar is dragged horizontally in GM to mimic the situation in a RFT model and the forces perpendicular and parallel to the longitudinal direction of the bar are recorded experimentally.

2.3. Bar drag experiment

An experimental setup as shown in Fig. 3a is used for force recording in locomotion dynamic analysis. A bar is submerged in GM at a specific depth and dragged by a sliding table fixed to a synchronous belt. The belt is driven by a stepping motor at a constant speed in the range of 1–100 cm/s. The angle between the longitudinal direction of the bar and the dragging direction can be conveniently adjusted by a dividing plate beneath the sliding table. A six-dimensional force sensor is mounted between the dividing plate and a vertical rod that is connected to the bar to record the forces exerted on the bar while dragging in dry sand. The sand used in the experiment is obtained from river banks that mixed three types of sand at a mixing ratio of 6:5:1. These sand samples are with particle diameters (PDs) of about 0.56 mm, 0.28 mm, and 0.125 mm, respectively. The average particle diameter (APD) is about 0.41 mm and the bulk density (the ratio of the mass and the volume, γ) is 1.3454 g/cm^3. The experiment is carried out in a glass tank of 1100 cm × 50 cm × 30 cm (i.e., 2683 APD × 1220 APD × 732 APD), which is large enough to eliminate the boundary effect of the tank on experimental result. The sand particles filled the tank are fully combed and flattened in order to maintain the same γ before each measurement. The bar is designed to have a trapezoidal cross section, with its length 10 times greater than its width. This design simplifies the force estimation on the stress surface by subtracting the forces on two end surfaces of the bar and neglecting the forces applied on the upper and the lower inclined surfaces (Lee and Herrmann, 1999).

As shown in Fig. 3b, the forces are recorded at different test conditions during the bar dragged in the GM. The measured forces demonstrate periodic fluctuations due to the elastic compression of sand below the critical failure point and the rapid destruction of sand above it. These fluctuating forces are averaged within a specific window in order to study the correlation of the forces with respect to the dragging angle and depth (Fig. 3d and e). In the experiment, the lift force in the z-axis direction F_z, the force normal to the stress surface $F_\perp$, and the force along the stress surface $F_\parallel$ (Fig. 3B) were measured with various ψ, which is set as an array with 4.5° interval in the range of 0°–90°. F_z caused by drag in horizontal direction was observed at different ψ, and increased with the increase of ψ (Fig. 3c), which was also analyzed in Ding et al. (2011), and this inspired the establishment of our failure-based model, which will be discussed in detail bellow. $F_\perp$ presents an upward trend in the entire range, for the bar needed to push away more sand blocking its way as ψ

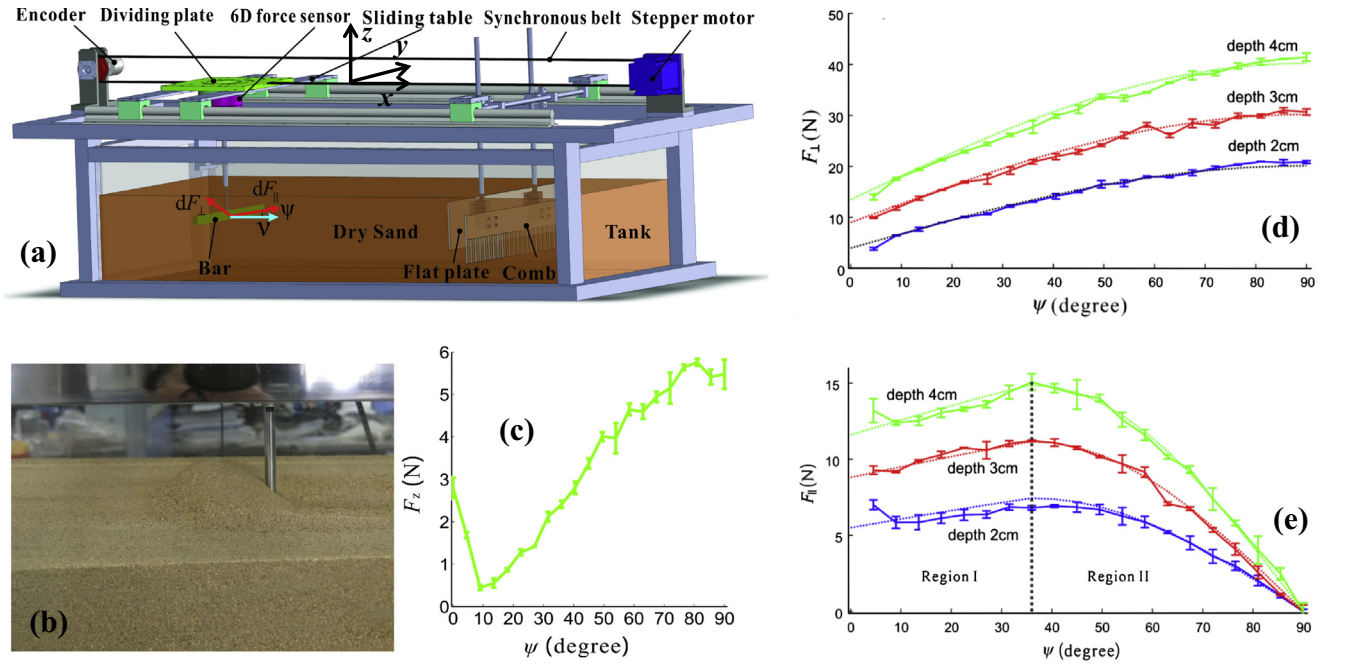

Fig. 3. Bar drag experiment performed to predict the forces on the element in Eq. (2). (a): Schematic of the experimental setup, v is the velocity of the bar. $F_\perp$ and $F_\parallel$ represent the normal force and the tangential force on the bar, respectively. Angle ψ between $F_\parallel$ and v is adjustable with a 4.5° resolution. F_z denotes the lift force caused by horizontal drag. (b): An example of the bar dragged in the GM. (c): Average F_z measured at different ψ at depth of 2 cm. (d): $F_\perp$ and (e): $F_\parallel$ measured in the experiment with respect to ψ at depth of 2 cm, 3 cm, 4 cm. Dashed lines are model fits described by Eqs. (3) and (4). The bar was dragged at a constant speed of 1 cm/s. Due to the influence of connecting cylinder at the back of the bar, the data recorded at $\psi = 0°$ and $\psi = 4.5°$ are biased.

increased (Fig. 3d). The situation of $F_\parallel$ is relatively complex (Fig. 3e), which is affected by the sands on the front of the bar and $F_\perp$. The flow of the sands on the front of the bar becomes few that decrease $F_\parallel$ as ψ increases; while the increase of $F_\perp$ will raises $F_\parallel$ by increasing friction. In Region I (ψ is less than 36°), $F_\parallel$ increases slowly for the dominant influence of $F_\perp$, however, afterward, it decreases more rapidly for the dominant influence of sand flows, which offsets the impact brought by $F_\perp$ and finally determines its zero value when ψ equals 90° (Region II). With the bar drag experiment, the forces on the bar with various ψ at certain depths can be obtained. Then, the key is that the trends of $F_\perp$ and $F_\parallel$ are applicable at the conditions of any depth and any speed.

Based on the above analysis, we developed an empirical fitting model describes the relationship between the forces and angle ψ. $F_\perp$ on the bar (excluding two end surfaces) can be written as

$$F_\perp = C_\perp^h + \left(C_\perp - C_\perp^h\right)\sin\psi \tag{3}$$

$F_\parallel$ in Region I and II can be respectively approximated as

$$\begin{aligned} F_\parallel^I &= C_\parallel^h + \left(C_\parallel - C_\parallel^h\right)\sin\psi \\ F_\parallel^{II} &= C_\parallel \cos\psi \end{aligned} \tag{4}$$

where $C_\perp^h$ and $C_\parallel^h$, describes depth dependent components in $F_\perp$ and $F_\parallel$ at $\psi = 0°$, respectively. $C_\perp$ and $C_\parallel$ represent the maximum $F_\perp$ and $F_\parallel$ can reach, which occur at $\psi = 90°$ and $\psi = 36°$ in our experiment, respectively. We found that there exists a nearly constant ratio between $C_\parallel$ and $C_\perp$, which equals 0.37 ± 0.02 through a lot of experiments. Considering $C_\perp$'s important role in the determination of the curves, and the value of $C_\perp$ varies along with the depth of the bar, we adopted a failure-based model to obtain them.

2.4. Failure-based model

Here we propose a failure-based model to obtain $F_\perp$ when ψ equals 90° at various depths. When ψ equals 90°, theoretically, $F_\parallel$ should be zero, while $F_\perp$ should reach its maximum for the bar pushes the most amount of sand blocking its way in the situation. Taking into account of sand forced movement in bar drag experiment, the top surface of sand bulging in front of the bar and then subsiding, a failure-based model was proposed. As shown in Fig. 4, the GM surrounding the bar is divided into two regions. For the sand in triangular region (ABC), just in upper front of the bar, it subsides quickly, filling the space caused by the movement of the bar, and can be regarded in active failure state, while the sand in trapezoidal region (ACDE) contributes to the bulge can be regarded in passive failure state (Ciamarra et al., 2004).

Assuming unit-distance in z direction, W_1 and W_2 can be expressed as

$$W_1 = \frac{\gamma}{2}h_1^2\cot\alpha_1, \quad W_2 = \frac{\gamma}{2}\left((h_0+h_1)^2\cot\alpha_2 - h_1^2\cot\alpha_1\right) \tag{5}$$

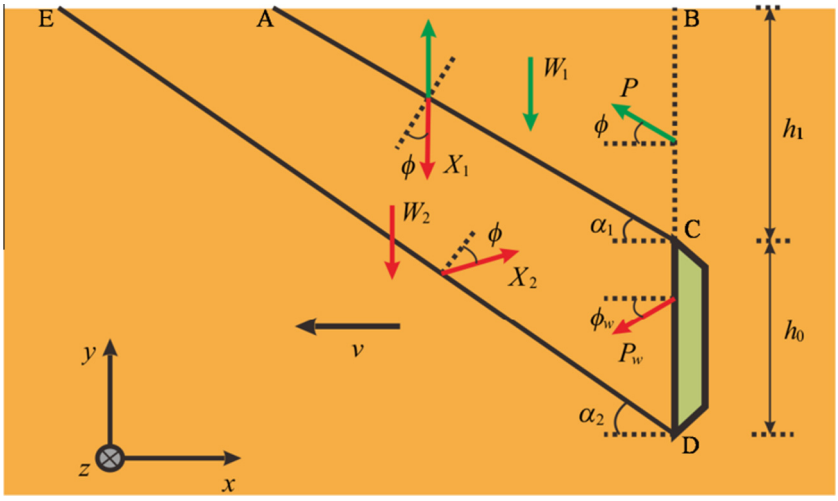

Fig. 4. A failure-based model to calculate $F_{\perp}$. W_1 and W_2 are the weight of GM in active failure and passive failure state, respectively. P denotes the force between sands in region ABC and outside, while P_w denotes force between the bar and sands in region ACDE. X_1 and X_2 represent the forces between sands in regions ABC and ACDE, and sands in region ACDE and below, respectively. ϕ is the friction angle within sand and ϕ_w is the friction angle between sand and the bar, which can all be measured by shear tests. h_1 denotes the distance between the surface of the sand and the top edge of the bar. h_0 represents the width of the bar. AC and DE represent the active failure plane and passive failure plane, respectively, α_1 and α_2 represent the angles between the active and passive failure plane and x-axis negative direction, respectively.

Assuming that the bar is dragged in a low speed, i.e. the active failure region and the passive failure are in quasi-static state, the equilibrium equation of the forces for the active failure region can be resolved horizontally and vertically

$$P\cos\phi - X_1\sin(\alpha_1-\phi)=0 \quad P\sin\phi + X_1\cos(\alpha_1-\phi)=W_1 \tag{6}$$

Solving Eq. (6), yields

$$P=\frac{\gamma h_1^2}{2\cos\phi}f(\alpha_1) \tag{7}$$

$$X_1=\frac{\gamma h_1^2}{2\sin(\alpha_1-\phi)}f(\alpha_1) \tag{8}$$

where

$$f(\alpha_1)=\frac{\cot\alpha_1}{\tan\phi+\cot(\alpha_1-\phi)}$$

For the passive failure region, resolving forces horizontally and vertically gives

$$\begin{aligned} &X_2\sin(\alpha_2+\phi)-X_1\sin(\alpha_1-\phi)-P_w\cos\phi_w=0\\ &X_2\cos(\alpha_2+\phi)-X_1\cos(\alpha_1-\phi)-P_w\sin\phi_w=W_2 \end{aligned} \tag{9}$$

Solving Eq. (9), gives

$$P_w=\frac{[W_2\sin(\alpha_2+\phi)+X_1\sin(\alpha_2-\alpha_1+2\phi)]}{\cos(\phi_w+\alpha_2+\phi)} \tag{10}$$

The change curve of P in the state of active failure is depicted as blue solid line in Fig. 5. Without disturbance, P locates in stable zone. Once the bar is dragged, P decreases toward $P_{\max}$ to reach active failure zone, at which P reaches $P_{\max}$ when α_1 equals $\alpha_{\max}$. The change curve of P_w in the state of passive failure is depicted as

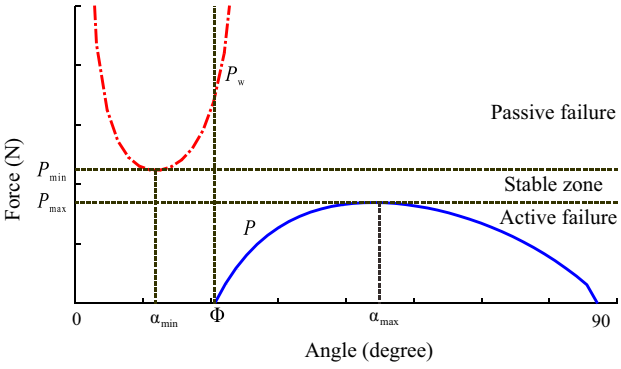

Fig. 5. Force in active failure zone, passive failure zone, and stable zone of GM.

red dashdot line in Fig. 5. Without disturbance, P_w also locates in stable zone. When the bar is dragged, P_w increases toward $P_{\min}$ to reach passive failure zone, which result in failures in different planes. Combined with the characteristics of the curves of both failures, motion can be considered to occur at the critical points in the same time roughly, thus P reaches $P_{\max}$ when α_1 equals $\alpha_{\max}$ and P_w reaches $P_{\min}$ when α_2 equals $\alpha_{\min}$, if the bar is dragged at a low enough speed. A detailed explanation of the active failure and the passive failure refers to Nedderman's work (Nedderman, 2005)

According to the above analysis, the value of α_1 can be obtained by setting $dP/d\alpha_1=0$, which gives

$$\alpha_{\max}=\arctan\left(\tan\phi+\sec\phi/\sqrt{2}\right) \tag{11}$$

Under this condition, substituting Eqs. (5), (8), (11) into (10), $\alpha_{\min}$ can be also obtained by the same way through setting $dP_w/d\alpha_2=0$, where $\alpha_{\min}$ is easy to obtain through

numerical analysis even though the differential form is too complex to be solved analytically. Hence, the force F_w acting horizontally to facing sand plane (CD in Fig. 4) can be deduced as $F_w = P_w \cos\phi_w$. With the failure-based model above, the parameters in the empirical fitting model described by Eqs. (3) and (4) can be conveniently obtained. As shown in Fig. 3d and e, the fitting result and the drag experiment corresponds well. Thus $F_\perp$ and $F_\parallel$ at any depth can also be obtained by changing h_1 (Fig. 4). Noting that both types of failure and the derivation of the forces are only suitable to the case of low-speed dragging, the calculation of $F_\perp$ and $F_\parallel$ would be extended to high-speed situations in next section.

2.5. Hybrid force model

Due to the difference in the magnitude and direction of the speed at each element (Fig. 2) as well as the speed range determined by the angular velocity of curved leg ω, the influence of speed cannot be ignored in the improved RFT, which is different from previous research in low speed cases (Albert et al., 1999; Chehata et al., 2003). According to the similar trends of $F_\perp$ and $F_\parallel$ observed in the bar drag experiment with different drag speeds, a convenient method to take ω into account is introduced. $F_\perp$ was measured when ψ equals 90° at different speeds from 1 cm/s to 100 cm/s at a certain depth. The interpolation result can be used to obtain the proportional relationship of the forces on the bar at different speeds with the same depth (Fig. 6). By substituting Eqs. (3) and (4) into Eq. (2) and combining the failure-based model and the relationship expressed in Fig. 6, the force and torque acting on the leg at any certain moment can be obtained by numerical computation.

In the hybrid force model, one important assumption is that the bulk density γ of the GM keeps constant during the leg penetration. However the assumption will lead to smaller forces and torque in prediction, especially for the supportive force. When the leg penetrates downward into the GM, γ increases with depth due to gravity and compact effect by the leg motion. The heterogeneity of the GM leads to increase of the forces, most obviously in the supportive force F_s. Considering this, the actual force $C_\perp$ should be greater than the model-predicted force F_w. Therefore, a calibration coefficient k is applied in the revised model to take heterogeneity into consideration. k represents the effect brought by variation of the bulk density that is relevant to the maximum penetration depth of the curved leg in the GM, Δd. The relationship can be represented as follows: $k = \lambda \Delta d$. Here λ denotes the constants for the forces despite the leg shapes, which is set as 0.0325 for the forward force and 0.06 for the supportive force, respectively.

2.6. Fixed axle rotation experiment

In order to validate the hybrid force model for the locomotion in granular media, we design and conduct an experiment to rotate curved legs with a fixed axle. The experiment setup is shown in Fig. 7. A six-dimensional force sensor is mounted between step motor and the curved leg record the forces exerted on the curved leg while rotating in dry sand. The force sensor was connected to the motor by a coupling. Z axle of the force sensor coincides with the leg's rotation axle. In this way, the torque T can be directly measured. The forces, F_f and F_s can also be obtained by decomposing two dimensional forces on the sensor along the direction of the forward force and the supportive force at each moment. Note that, before penetrating in sands, the curved legs rotate in air first. The measured forces and torque in air will be saved as the influence of inertia forces. After the experiment of corresponding legs rotating in sands, and the forces and torque will be processed to eliminate the influence of inertia forces. The sand used in the experiment is same as that in the bar-drag experiment. The sand particles filled the tank are fully combed and flattened in order to maintain the same γ before each measurement.

In the experiment, the influence of the shape of the curved legs and that of the rotation speed could be explored by switching the curved legs and altering the driving speed of the step motor. To reveal the influence of the

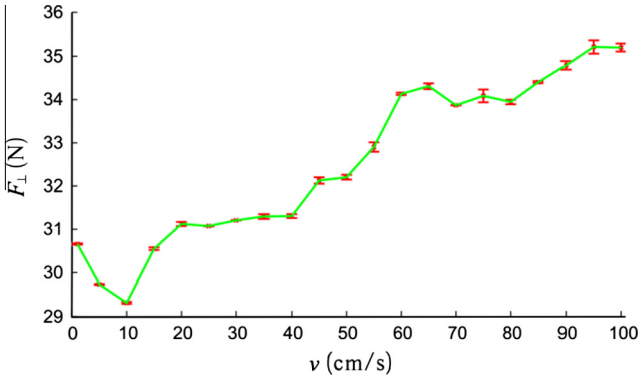

Fig. 6. $F_\perp$ as a function of bar speed v in the range of 1–100 cm/s at depth 3 cm, with ψ equaling to 90°. The green solid line is the interpolation result used in improved RFT. (For interpretation of the references to colour in this figure legend, the reader is referred to the web version of this article.)

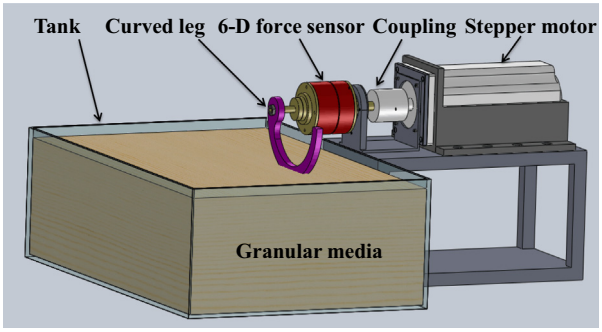

Fig. 7. Fixed axle rotation experiment performed to validate the forces calculated in the hybrid force model.

leg shape on the locomotion performance of robots in GM, five types of legs as shown in Fig. 8 are adopted for experiment. The vertical axis of these five elliptic legs, a, keep constant, while the other axis, b, varies to form different leg shapes. Leg I simulates the situation of a straight leg, Leg V simulates the situation of very bent leg, and Leg III is the semi-circle leg used in RHex series robots and AmphiHex-I (Saranli et al., 2001; Liang et al., 2012). Despite the shape of the legs, the influence of angular velocity of the legs is also explored. The angular velocity of the leg is set below 11 rad/s. This working range is limited by the parameters such as the maximal speed of the dragged bar and the shape of the leg.

3. Results and discussion

With the above hybrid model and experimental setup, the leg–GM dynamics in the entire rotating period of the curved leg can be obtained and analyzed. Here the influenced of the angular velocity and the shape of the curved legs are explored by the model and experiment, simultaneously.

3.1. Influence of angular velocity

The influence of various angular velocities on the forces and the torque acting on semi-circle leg is explored. The dynamic characteristics of the forces and the torque during a single period of leg penetration are obtained from the hybrid model and the corresponding experiments, respectively. These simulated force and torque profiles are in coincident with the corresponding experimental results, as plotted in Fig. 9. Based on the results, it is obvious that the semi-circle leg overcomes the existing limitations of wheels or straight legs by providing both relatively large propulsive and supportive forces. In addition to the propulsive and supportive forces, torque T also plays an important role in amphibious robot locomotion. For a constantly rated power of the motor, the output torque is inversely proportional to the angular velocity ω.

An interesting observation from Fig. 9 is that the angular velocity ω has a negligible influence on the forces and the torque within the working range below 11 rad/s. A reasonable explanation for this observation is that the shape of the leg undermines the effect of the angular velocity ω on the forces and the torque. Consequently, the shape of the leg is the major contributing factor that affects the performance of a terrestrial robot in GM under the same granular condition and the same height h. Thus, we set the angular velocity of 1 rad/s in the following study for the convenience of analysis.

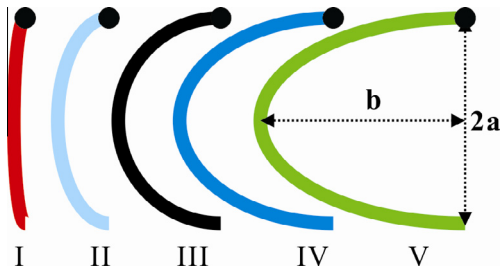

Fig. 8. Five types of curved leg with various relative magnitudes of a and b. I: straight leg ($a = 9b$), II: less straight leg ($a = 2b$), III: semi-circle leg ($a = b$), IV: bent leg ($a = 0.67b$), V: very bent leg ($a = 0.5b$).

3.2. Influence of leg shape

For the different leg shapes, the dynamic characteristics of the forces and the torque during a single period of leg penetration are numerically simulated and experimentally tested, as presented in Fig. 10, respectively. The coincidence between the simulated and the tested results verifies the effectiveness of the hybrid model. According to the figures, the force and the torque profiles show similar peaks for different leg shapes except that the peaks occur at different angular positions with different magnitudes for few cases. F_f and F_s are relatively small in the case of a straight leg. As b increases, F_f and F_s increase monotonically till the case of a semi-circle leg. As the leg shape changes from a semi-circle (i.e., $a = b$) to a bent shape (i.e., $a < b$), F_f and F_s peak at different angular positions but remain relatively constant amplitudes. As b increases further, both the peak positions and the peak amplitudes of the forces change significantly with the leg shape. By comparing the profiles of F_f and F_s in Fig. 10, it is noted that the phase of the F_s peak is always ahead of that of the F_f peak for the same leg shape. This can be explained by the earlier penetration effect in the vertical direction than that in the horizontal direction. Fig. 10(c) and (f) shows that the motor should provide a larger torque to penetrate GM as b increases. However, the very bent leg affects T negatively, set a greater power requirement for the driving motor, and its effect should be considered in the locomotor design. Fig. 11 shows the combinatory effect of the leg shape on F_f/T and F_s/T. For an optimal locomotion performance, it is desirable to increase F_f and F_s while reduce T. According to Fig. 11, changing the leg shape from a straight leg to a semi-circle leg improves the locomotion performance. However, further increase of b to a bent leg shape increases F_f/T but reduces F_s/T. In the extreme condition of a very bent leg, the locomotion performance becomes very poor. This result will provide an effective guidance for the leg type selection in the design of amphibious robots and desert robots.

4. Discussion

For the different leg shapes, the moments that the legs begin to penetrate GM vary, while the moments that the legs leave GM are same thanks to the semi-elliptical shape of the legs, which is shown in Fig. 10. However, the forces acting on different legs shows great difference when they leave GM. For example, the forces acting on the very bent leg approach zero long before the leg leaves the GM than

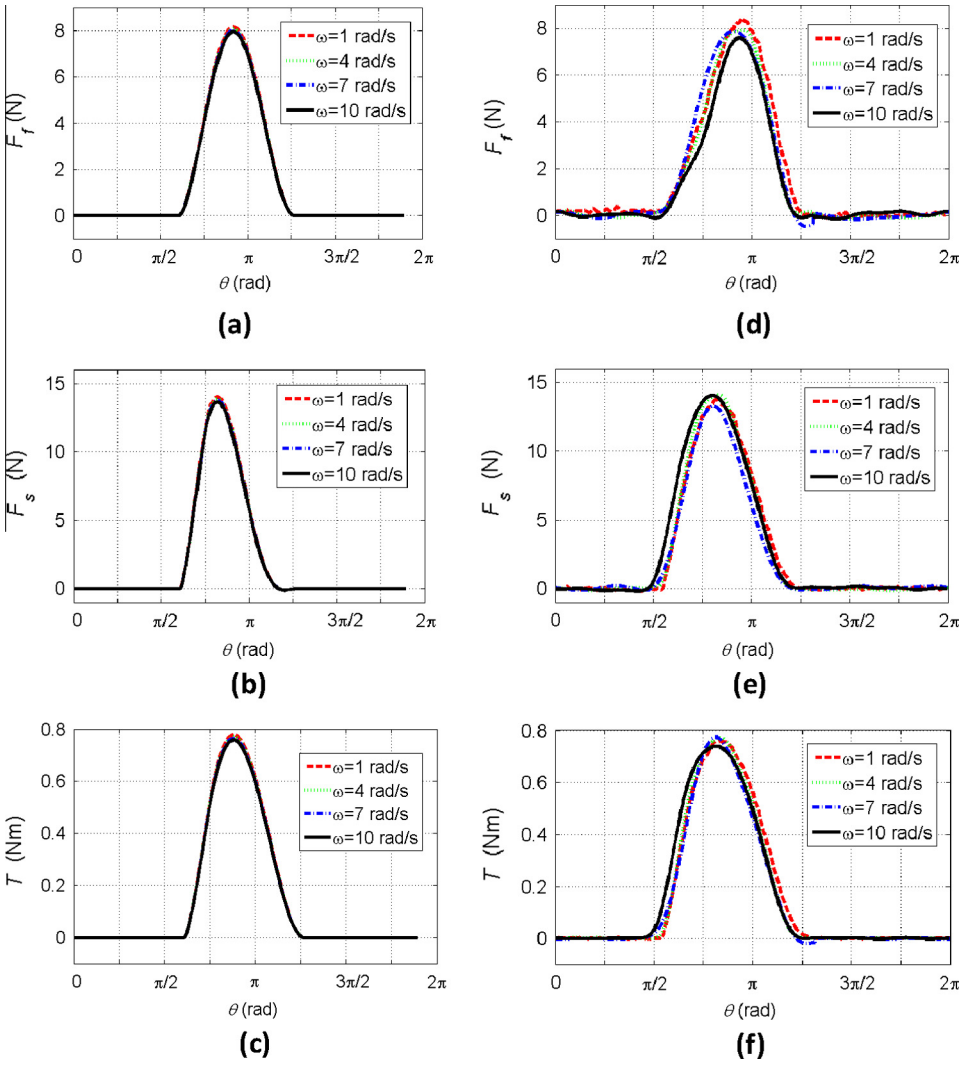

Fig. 9. Forces and torque of semi-circle leg obtained from the hybrid model and the corresponding experiment during one penetration period, respectively. Here $a = b = 4.5$ cm, $h = 5$ cm, and ω equals 1 rad/s, 4 rad/s, 7 rad/s and 10 rad/s, respectively. Angular velocity ω is chosen according to the maximum speed we performed in bar drag experiment and the maximum speed of the element of the leg. Solid lines and dashed lines denote the data obtained from the model and the experiment, respectively: (a)–(c): forward advancing force, F_f, supportive force, F_s, and torque, T from the model. (d)–(f) forward advancing force, F_f, supportive force, F_s, and torque, T from the experiment.

others do. The phenomenon could be explained by Fig. 12, which shows the correlation between the angle measured counterclockwise from the chord of an leg element to the leg axial diameter a (denoted as ξ) and the angle measured counterclockwise from speed v to tangential direction of the leg element (denoted as ψ). A negative ψ corresponds to the situation where the leg element is in contact with the surrounding GM and contributes to the locomotion dynamics. According to Fig. 12, ψ is always negative for the leg shapes from a straight leg to a semi-circle leg. However, a positive ψ occurs as ξ approaches to 0 rad in the cases of the bent and the very bent legs. A positive ψ means the leg elements do not contribute to the leg–GM interaction because the granular particles have been pushed away by the neighboring leg elements with leg–GM interactions in advance. The portion of the leg elements without contribution to the locomotion dynamics increases as the axial diameter b increases, leading to the rapid decline of F_f, F_s and T for the bent and the very bent leg shapes, as shown in Fig. 10.

Though the model can nearly reflect the actual situations, some differences between the estimation of the model and experimental result still need to be discussed. Firstly, the estimation of a large negative for F_s of straight leg mainly results from the simplification in hybrid force model, that is we just use the forces measured from bar dragged in a horizontal plane to simulate the forces of leg penetration in a vertical plane. The simplification may be correct if the interaction between the leg element and the GM occurs relative deeply, while it is inaccurate when the interaction occurs at a smaller depth. The error becomes more obvious in the case of straight leg. Secondly, a slightly smaller value predicted especially in F_s of the very bent leg, comes from the assumption that compaction rate

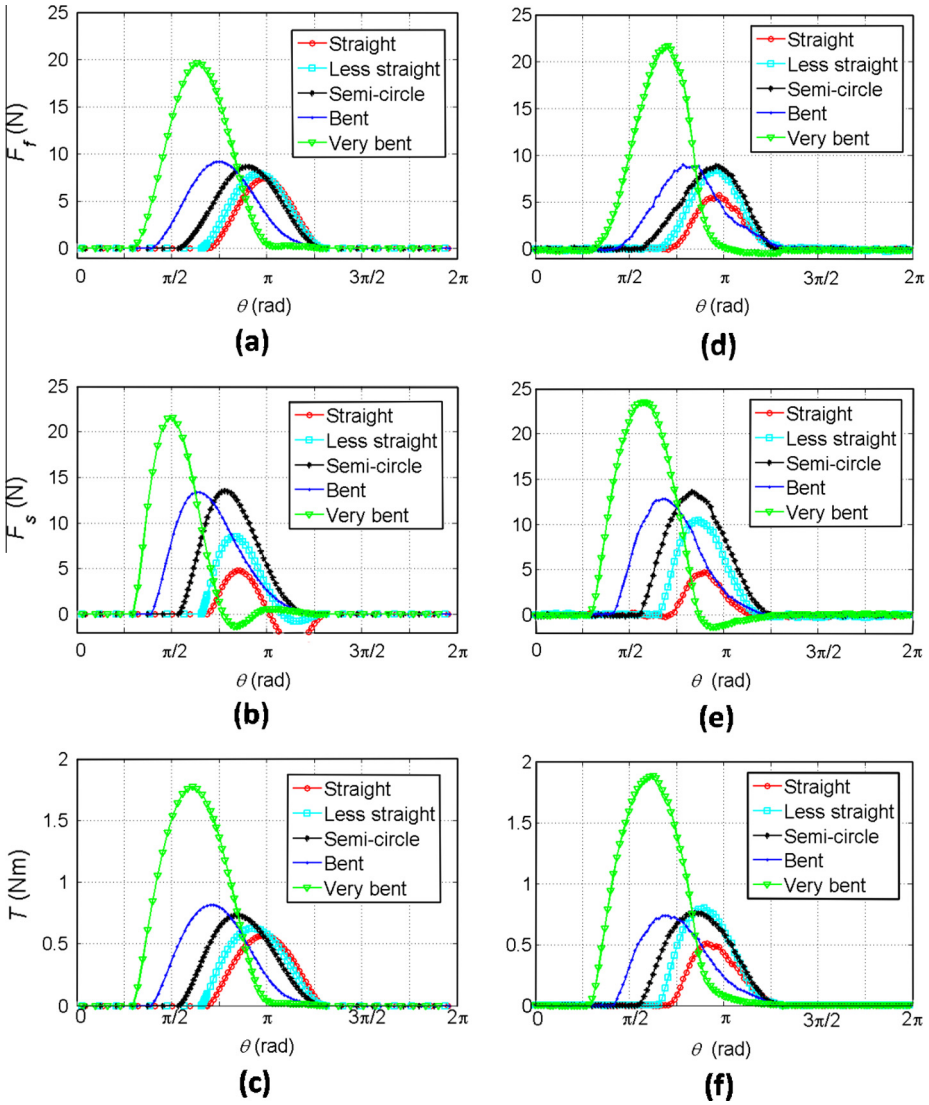

Fig. 10. Forces and torque acting on the five types of legs obtained from the revised hybrid model and the corresponding experiments during one penetrating period, respectively, here ω equals 1 rad/s. Solid lines and dashed lines denote the data obtained from the model and the experiments, respectively. (a)–(c): forward advancing force, F_f, supportive force, F_s, and torque, T from the hybrid model. (d)–(f) forward advancing force, F_f, supportive force, F_s, and torque, T from the experiment.

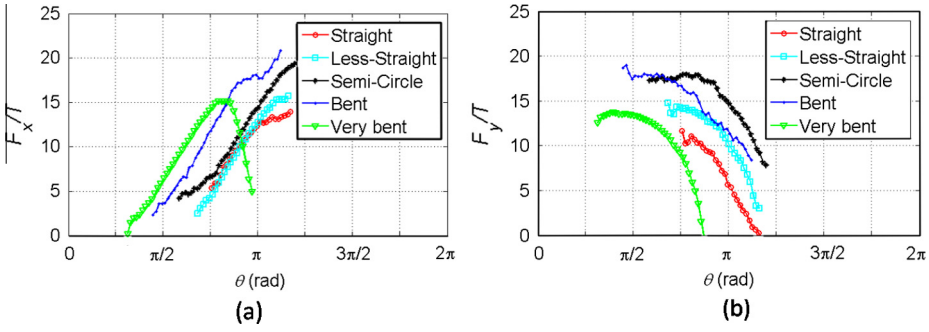

Fig. 11. Ratios of (a) F_f to T and (b) F_s to T obtained from experiment during one rotation period in different leg type cases. Note that the value when torque is too small is eliminated to remove the disturbance of noise.

of the GM varies according to the maximum penetration depth of the legs. However, the compaction rate is relevant to more factors such as the penetrating volumes and the penetration direction, which leads to a small deviation for the case of very bent leg. Despite inaccuracy in some special cases, the trends and correlations show a good

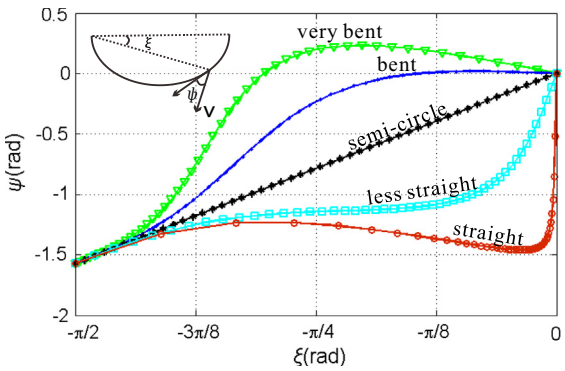

Fig. 12. ψ as a function of ξ in different leg cases. Inset: ξ is the angle measured counterclockwise from the chord of an leg element to long axis a. ψ is the angle measured counterclockwise from speed v to tangential direction of the leg element.

consistence between the result from the hybrid model and the experiments, which is meaningful when leg types are determined or control strategy is chosen in developing a field robot locomoting in desert or amphibious environment.

According to the above analysis, very bent leg should be adopted when the substrate is very loose and energy is not a limiting factor, where F_f and F_s are the main factors determining the locomotion performance. Generally, by balancing the positive effect of forces and the negative effect of torque, as well as reducing the fluctuations of the center of mass, semi-circle leg or bent leg should be chosen. Considering human beings or animals, who are not necessary and are not able to afford so much energy to maintain intense power continuously, straight or less straight legs are also more beneficial, such as hatching sea turtles. The locomotion depends not only to the magnitude but also to the duration time of the forces. Thus, no matter what type of leg is chose, the duration of the forces and the torque, especially the peak positions should be fully utilized either in control strategy or in structural design. One effective method is to adopt a lower rotation speed in overlapping region of the two forces to extend the interaction time and reduce inertia force of robot body, while to adopt a higher speed in the region without contribution to $F_\perp$ and $F_\parallel$. Further consideration of the control strategy inevitably involves the weight and leg distribution of the robot, which would be explored in detail in future study.

RFT model was firstly introduced describe the propulsion of sea-urchin spermatozoa, and then was applied to explain sandfish's swimming in sand (Goldman et al., 2009). In the work, the RFT model can only solve problems of movement on an approximately plane, and give a satisfied result in a low speed situation. Compared to the work, we included the factor of bar velocity v and depth d besides angle ψ in our model, so the model can be used to explain force situation of variable depths and can deliver better prediction results for any profiles of locomotors. Recently, Li et al. extended the existing model to explain variable depth situation, which achieves great success for good predictions on the dynamics of robot locomotion in GMs (Li et al. (2013)). However, the model involves two angle parameters in vertical and horizontal planes simultaneously, which requires massive experiments to achieve the accurate forces on the elements of legs. In our model, we only consider one angle parameter ψ to make it easy to be measured with a relatively high accuracy. More importantly, with the simplified model, we can incorporate classic terramechanics such as the failure based model into the hybrid model on locomotion in GM. With the hybrid model, the force prediction becomes very easy by performing limited times of experiments conveniently.

5. Conclusion

In this paper, we proposed a hybrid force model to describe the dynamics of locomotors of any shape. A failure-based model explaining the situation that a bar is dragged at a low speed and any depth beneath the granular surface is proposed, which was further extended to high-speed cases by a simple calibration. Combined with improved RFT considering the factors of speed and depth, we estimated the dynamics of a newly designed locomotion mechanism, semi-elliptical leg, as well as predicted the performance influenced by the angular velocity and the shape of legs. The result provides an important reference for the design and control of the amphibious and terrestrial locomotors. It is worth motioning that the sand used in bar drag experiment is gathered beside a river, which emphasizes the practical value of the method rather than chooses homogeneous and regular particles as GM.

With the hybrid model, the forces between the legs and GM can easily be estimated and evaluated. The method applied in this paper can be considered to be extended to more types of complex substrates, such as wet sand, and so on. The most important significance is that the model makes it possible to predict dynamics on legs of complex shapes with a relative high accuracy, which is certainly tedious work when obtained by experiments. However, a lot of work has to be done before it can be widely used. At least, more effective methods to account for the effect of different compaction rate may be discussed in detail and be incorporated in the model. In practical applications, the weight of the robot should also be considered for more accurate prediction of the velocity, the efficiency, or other important assessment function of robot locomotion performance.

Acknowledgment

This research has been financially supported by National Natural Science Foundation of China (Nos. 51375468, 50975270).

References

Albert, R., Pfeifer, M.A., Barabási, A.L., Schiffer, P., 1999. Slow drag in a granular medium. Phys. Rev. Lett. 82 (1), 205–208.

Albert, I., Tegzes, P., Kahng, B., Albert, R., Sample, J.G., Pfeifer, M., et al, 2000. Jamming and fluctuations in granular drag. Phys. Rev. Lett. 84 (22), 5122–5125.

Asnani, V., Delap, D., Creager, C., 2009. The development of wheels for the lunar roving vehicle. J. Terramech. 46 (3), 89–103.

Bekker, M.G., 1956. Theory of Land Locomotion: The Mechanics of Vehicle Mobility. University of Michigan Press.

Bekker, M.G., 1969. Introduction to Terrain-Vehicle Systems. University of Michigan Press, Ann Arbor (MI).

Boxerbaum, A.S., Werk, P., Quinn, R.D., Vaidyanathan, R., 2005. Design of an autonomous amphibious robot for surf zone operation: Part I mechanical design for multi-mode mobility. In: Proceedings of IEEE/ASME International Conference on Advanced Intelligent Mechatronics. pp. 1459–1464.

Chehata, D., Zenit, R., Wassgren, C.R., 2003. Dense granular flow around an immersed cylinder. Phys. Fluids 15 (6), 1622–1631.

Ciamarra, M.P., Lara, A.H., Lee, A.T., Goldman, D.I., Vishik, I., Swinney, H.L., 2004. Dynamics of drag and force distributions for projectile impact in a granular medium. Phys. Rev. Lett. 92, 194301.

Crespi, A., Karakasiliotis, K., Guignard, A., Ijspeert, A.J., 2013. Salamandra robotica II: an amphibious robot to study salamander-like swimming and walking gaits. IEEE Trans. Robot. 29 (2), 308–320.

Ding, Y., Gravish, N., Goldman, D.I., 2011. Drag induced lift in granular media. Phys. Rev. Lett. 106 (2), 028001.

Ding, L., Gao, H., Deng, Z., Song, J., Liu, Y., Liu, G., et al, 2013. Foot–terrain interaction mechanics for legged robots: modeling and experimental validation. Int. J. Robot. Res. 32 (13), 1585–1606.

Ding, L., Deng, Z., Gao, H., Guo, J., Zhang, D., Iagnemma, K., 2013. Experimental study and analysis of the wheels' steering mechanics for planetary exploration wheeled mobile robots moving on deformable terrain. Int. J. Robot. Res. 32 (6), 712–743.

Dudek, G., Giguere, P., Prahacs, C., Saunderson, S., Sattar, J., Torres-Mendez, L.A., et al, 2007. Aqua: an amphibious autonomous robot. Computer 40, 46–53.

Fervers, C.W., 2004. Improved FEM simulation model for tire–soil interaction. J. Terramech. 41 (2), 87–100.

Gao, H., Li, W., Ding, L., Deng, Z., Liu, Z., 2012. A method for on-line soil parameters modification to planetary rover simulation. J. Terramech. 49 (6), 325–339.

Goldman, D.I., Komsuoglu, H., Koditschek, D.E., 2009. March of the sandbots. IEEE Spectr. 46, 30–35.

Gray, J., Hancock, G.J., 1955. The propulsion of sea-urchin spermatozoa. J. Exp. Biol. 32 (4), 802–814.

Iagnemma, K., Kang, S., Shibly, H., Dubowsky, S., 2004. Online terrain parameter estimation for wheeled mobile robots with application to planetary rovers. IEEE Trans. Robot. 20 (5), 921–927.

Janosi, Z., Hanamoto, B., 1961. The analytical determination of drawbar pull as a function of slip for tracked vehicles in deformable soils. In: Proceedings of the 1st International Conference on Soil–Vehicle Systems. Turin, Italy.

Kadanoff, L.P., 1999. Built upon sand: theoretical ideas inspired by granular flows. Rev. Mod. Phys. 71 (1), 435.

Knuth, M.A., Johnson, J.B., Hopkins, M.A., Sullivan, R.J., Moore, J.M., 2012. Discrete element modeling of a Mars Exploration Rover wheel in granular material. J. Terramech. 49 (1), 27–36.

Lee, J., Herrmann, H.J., 1999. Angle of repose and angle of marginal stability: molecular dynamics of granular particles. J. Phys. A: Math. Gen. 26 (2), 373.

Lejeune, T.M., Willems, P.A., Heglund, N.C., 1998. Mechanics and energetics of human locomotion on sand. J. Exp. Biol. 201 (13), 2071–2080.

Li, C., Umbanhowar, P.B., Komsuoglu, H., Koditschek, D.E., Goldman, D.I., 2009. Sensitive dependence of the motion of a legged robot on granular media. P. Natl. Acad. Sci. 106 (9), 3029–3034.

Li, C., Umbanhowar, P.B., Komsuoglu, H., Goldman, D.I., 2010. The effect of limb kinematics on the speed of a legged robot on granular media. Exp. Mech. 50 (9), 1383–1393.

Li, C., Zhang, T., Goldman, D.I., 2013. A terradynamics of legged locomotion on granular media. Science 339 (6126), 1408–1412.

Liang, X., Xu, M., Xu, L., Liu, P., Ren, X., Kong, Z., Yang, J., Zhang, S., 2012. The AmphiHex: a novel amphibious robot with transformable leg–flipper composite propulsion mechanism. In: IEEE/RSJ International Conference on Intelligent Robots and Systems (IROS). pp. 3667–3672.

Lighthill, M., 1969. Hydromechanics of aquatic animal propulsion. Annu. Rev. Fluid Mech. 1 (1), 413–446.

Liu, J., Kushwaha, R.L., 2010. Force transmitted below the soil surface by human gait. J. Terramech. 47 (5), 337–342.

Maladen, R.D., Ding, Y., Umbanhowar, P.B., Kamor, A., Goldman, D.I., 2011. Mechanical models of sandfish locomotion reveal principles of high performance subsurface sand-swimming. JR Soc. Interface 8 (62), 1332–1345.

Metcalfe, G., Tennakoon, S.G.K., Kondic, L., Schaeffer, D.G., Behringer, R.P., 2002. Granular friction, Coulomb failure, and the fluid–solid transition for horizontally shaken granular materials. Phys Rev E 65 (3), 031302.

Nedderman, R.M., 2005. Statics and Kinematics of Granular Materials. Cambridge University Press.

Patel, N., Ellery, A., Allouis, E., Sweeting, M., Richter, L., 2004. Rover mobility performance evaluation tool (RMPET): a systematic tool for rover chassis evaluation via application of Bekker theory. In: Proceedings of the 8th ESA Workshop on Advanced Space Technologies for Robotics and Automation. pp. 1–8.

Percier, B., Manneville, S., McElwaine, J.N., Morris, S.W., Taberlet, N., 2011. Lift and drag forces on an inclined plow moving over a granular surface. Phys. Rev. E 84 (5), 051302.

Raibert, M., Blankespoor, K., Nelson, G., Playter, R., 2008. Bigdog, the rough–terrain quadruped robot. In: Proceedings of the 17th World Congress. pp. 10822–10825.

Saranli, U., Buehler, M., Koditschek, D.E., 2001. RHex: a simple and highly mobile hexapod robot. Int J Robot Res 20 (7), 616–631.

Scott, G.P., Saaj, C.M., 2012. The development of a soil trafficability model for legged vehicles on granular soils. J. Terramech. 49 (3), 133–146.

Senatore, C., Wulfmeier, M., Vlahinic, I., Andrade, J., Iagnemma, K., 2013. Design and implementation of a particle image velocimetry method for analysis of running gear–soil interaction. J. Terramech. 50 (5), 311–326.

Smith, W., Peng, H., 2013. Modeling of wheel–soil interaction over rough terrain using the discrete element method. J. Terramech. 50, 277–287.

Terzaghi, K., 1943. Theoretical Soil Mechanics. Wiley, New York.

Xia, K., 2011. Finite element modeling of tire/terrain interaction: application to predicting soil compaction and tire mobility. J. Terramech. 48 (2), 113–123.

Xu, L., Liang, X., Xu, M., Zhang, S., 2013. Interplay of theory and experiment in analysis of the advantage of the novel semi-elliptical leg moving on loose soil. In: IEEE/ASME International Conference on Advanced Intelligent Mechatronics. pp. 26–31.

Yang, Y., Sun, Y., Ma, S., Yamamoto, R., 2014. Characteristics of normal and tangential forces acting on a single lug during translational motion in sandy soil. J. Terramech. 55, 47–59.

Yeomans, B., Saaj, C.M., Van Winnendael, M., 2013. Walking planetary rovers – experimental analysis and modelling of leg thrust in loose granular soils. J. Terramech. 50 (2), 107–120.

Zhang, S., Liang, X., Xu, L., Xu, M., 2013. Initial development of a novel amphibious robot with transformable fin–leg composite propulsion mechanisms. J. Bio. Eng. 10 (4), 434–445.